2-D Companding for Noise Reduction in Strain Imaging

Pawan Chaturvedi, *Member, IEEE*, Michael F. Insana, *Member, IEEE*, and Timothy J. Hall, *Member, IEEE*

Abstract—Companding is a signal preprocessing technique for improving the precision of correlation-based time delay measurements. In strain imaging, companding is applied to warp 2-D or 3-D ultrasonic echo fields to improve coherence between data acquired before and after compression. It minimizes decorrelation errors, which are the dominant source of strain image noise. The word refers to a spatially variable signal scaling that compresses and expands waveforms acquired in an ultrasonic scan plane or volume. Temporal stretching by the applied strain is a single-scale (global), 1-D companding process that has been used successfully to reduce strain noise. This paper describes a two-scale (global and local), 2-D companding technique that is based on a sum-absolute-difference (SAD) algorithm for blood velocity estimation. Several experiments are presented that demonstrate improvements in target visibility for strain imaging. The results show that, if tissue motion can be confined to the scan plane of a linear array transducer, displacement variance can be reduced two orders of magnitude using 2-D local companding relative to temporal stretching.

I. INTRODUCTION

ELASTICITY IMAGING describes a broad range of emerging techniques for visualizing mechanical properties of soft biological tissues in vivo [1]–[13]. Static methods use an ultrasound transducer in place of a physician's hand to palpate tissues and detect stiff objects located below the skin surface [6]–[8]. The transducer/compressor combination becomes a remote sensing device for imaging tissue strain deep in the body. Strain images provide unique diagnostic information because of the large stiffness contrast that exists between some normal and diseased tissues [14], [15].

Strain images are generated by comparing ultrasound scans—specifically, the radio-frequency echo fields—acquired before and after compression of the tissue surface. Internal tissue displacements are tracked along the beam axis by classical 1-D time delay estimation [19], [20] applied to segments of pre- and postcompression echo waveforms. A strain image is computed from the gradient of the displacement field.

Visibility of targets in strain images is currently noise limited [16], where the strain noise is determined by the displacement covariance. Displacement covariance has two sources: signal-independent ultrasound noise and signal-dependent decorrelation noise [18]. The loss of coherence between pre- and postcompression echo fields is the dominant source of displacement error in strained signals.[1] Displacement variance increases nonlinearly with the amount of applied strain [18]–[23]. However, when the deformation occurs only in the scan plane, prior knowledge of the strain can be used to warp 2-D echo fields to restore echo field coherence for time delay estimation and thereby reduce strain noise [22], [23].

Previously, strain noise was maintained at acceptable levels by compressing the tissue only a small percentage of its total height ($\leq 1\%$) [7], [16]. After compression, the echo field was linearly stretched along the beam axis by the average applied strain before crosscorrelation with the precompression echo field [24]. Temporal stretching [16], [17], known as companding in the signal processing literature [23], reduces strain noise by restoring coherence between the waveforms to be crosscorrelated. Because crosscorrelation methods assume there is only rigid-body motion over the duration of the data window, stretching signals by the applied strain conditions the data to better satisfy this critical assumption. The improvement in strain noise depends on the duration of the data window, the elastic heterogeneity of the medium, and the amount of strain [18].

Strain is estimated in one dimension only, along the beam axis, because the axial sampling interval is often 10 times finer than the lateral sampling interval. (For example, a 5 MHz linear array sampled at 50 Msamples/s has a 15 μm axial sampling interval. The echo line density for this array was 5/mm, producing a lateral sampling interval of 200 μm.) High sampling rates are needed for strain imaging to reduce the demands on interpolation algorithms for detecting correlation peaks using digitized echo data. Interpolation can increase displacement variance and bias [26]. Unfortunately, biological tissues do not move in one dimension when compressed, and temporal stretching is insufficient to avoid decorrelation errors. Temporal stretching may be extended to two or three dimensions by establishing known boundary conditions and assuming the medium is homogeneous and incompressible [25], but it is rare that these assumptions are valid at all spatial scales for biological tissues.

Multicompression displacement estimators have been proposed to minimize decorrelation errors [8], [24], [31],

The authors are with the Department of Radiology, University of Kansas Medical Center, Kansas City, KS 66160–7234 (e-mail: insana@research.kumc.edu).

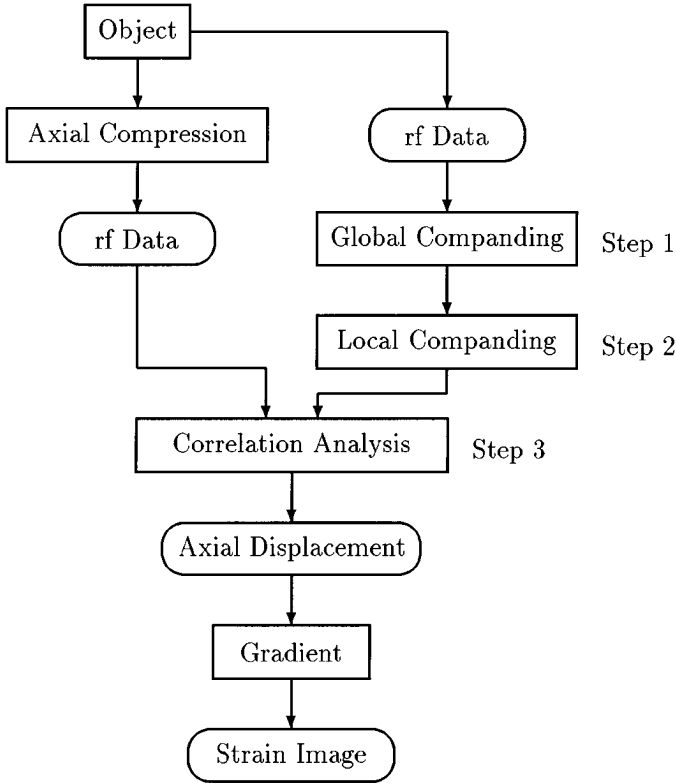[1]Strained signals are those with time-varying time delay.

Fig. 1. A flow chart summarizing the proposed algorithm to form strain images.

[32]. These methods combine displacements estimated from many small compressions to increase object contrast for strain while minimizing decorrelation errors. Although multicompression approaches achieve their objective, they are also susceptible to registration error, are of limited use in cases of low echo signal-to-noise ratio, and require large data volumes and long acquisition and computation times. Alternatively, the 2-D companding methods described below provide uniformly low strain noise in elastically heterogeneous media subjected to relatively large strains without the limitations of multicompression methods. However, it is more important for 2-D companding than multicompression methods that all motion occur in the scan plane.

The strategy proposed in this paper for strain imaging is diagrammed in Fig. 1. Boundary conditions are adjusted so that object motion is confined to the scan plane [33]. In a first-pass process, the medium is assumed to be incompressible, i.e., Poisson's ratio $\simeq 0.5$, and spatially uniform in elasticity. Global companding methods are applied to the echo fields in two dimensions to detect and adjust for large-scale (average) deformations and displacements. In a second-pass process, elastic heterogeneities in the medium are recognized at low resolution by a 2-D local companding technique. Echo waveforms are shifted correspondingly in directions axial and lateral to the beam. In a third-pass process, crosscorrelation is applied along the direction of beam propagation to measure the residual axial displacement. Axial measurements from steps 2 and 3 are added before taking the gradient to form the strain image. The

first two steps warp the 2-D precompression data field to match the postcompression field and improve waveform coherence point-by-point. The overall displacement variance is reduced because it is mainly determined by estimation errors in the third (crosscorrelation) step. In this way, mean displacement is preserved while its variance is reduced, so strain noise is controlled with minimal loss of image contrast. Notice that warping the precompression field to match the postcompression field is equivalent to warping the postcompression field to match the precompression field. We choose the former for convenience only. Also, alignment of the beam axis with respect to the axis of compression is critical to avoid misleading displacement information [28]–[30]. For this reason, linear arrays are used. Throughout the paper, we assume that compression results in a positive strain and expansion in a negative strain.

The 2-D companding process is described in the next section.

II. Methods

A. Observation of Motion Due To Compression

Consider an incompressible free-standing block of material that is compressed by a planar surface from above, along the z axis, and held fixed from below. The longitudinal strain, s_z, is in the direction of the applied stress; the transverse strains, s_x and s_y, are perpendicular to the applied stress; and $s_z = -2s_x = -2s_y$. Minus signs indicate that compression along z results in expansion in x, y.

In strain imaging, motion is always measured along the axis of the ultrasound beam where the spatial sampling rate is highest. Therefore, we study the object in compression by measuring the axial displacement to compute the longitudinal strain. Similarly we study the object in tension by measuring the axial displacement to compute the transverse strain. Longitudinal and transverse refer to the motion of a planar compressor, and in-plane (axial and lateral) and out-of-plane (elevational) refer to the beam axis of a 1-D array transducer. Notice that if the boundary conditions are set to prevent motion along x, then $s_x = 0$ and $s_z = -s_y$. In that case, in x, z at $y = 0$, virtually all motion is along z. Similarly, when the x, y boundaries are unconstrained and the y, z image plane is along the central plane of the block, virtually all motion is in the image plane.

B. Echo Fields

Strain images are formed by analyzing a precompression echo field $\mathbf{U}$ and postcompression echo field $\mathbf{C}$. Both are $Z \times Y$ dimensional matrices of samples from continuous echo waveforms (see Fig. 2). For example, $\mathbf{U} = (U_z, U_y)$, $z = 1...Z$, $y = 1...Y$, where there are Y waveforms each consisting of Z digitized echo values.

(a)   (b)

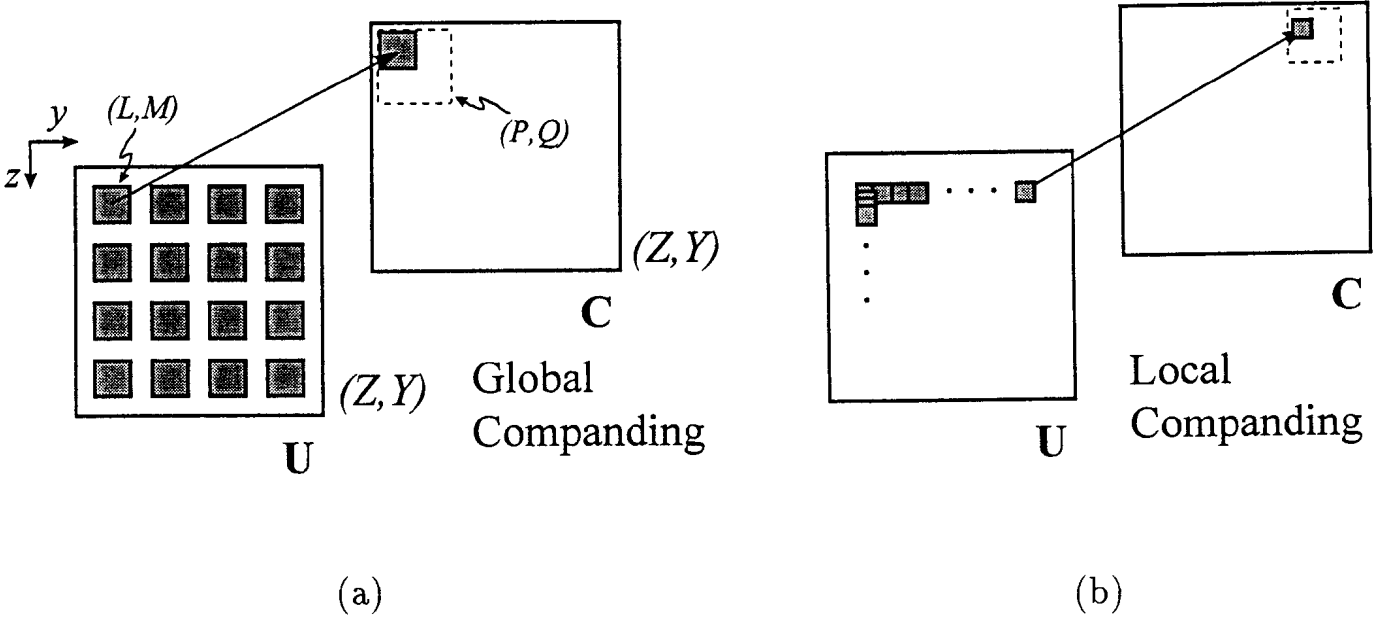Fig. 2. Division of the echo field into data kernels (shaded) for 2-D (a) global, and (b) local companding. **U** represents the uncompressed echo field matrix, **C** represents the compressed echo field matrix, and z, y is the image plane. For global companding, the echo fields are divided into 16 nonoverlapping kernels. For local companding, they are divided into 10^4 overlapping kernels for a 15 mm × 15 mm echo field. The data kernels for global companding are five times larger than those for local companding.

C. Sum-Absolute-Difference (SAD) Algorithm

The SAD algorithm, previously used for blood velocity estimation [34], [35], is the essence of companding. It is useful because it calculates displacements accurately at high speed. SAD provides performance similar to correlation for 2-D displacement estimation but requires eight-times fewer arithmetic operations [34].

SAD is implemented by selecting corresponding data kernels from **U** and **C** of size $L \times M$. Then for all (i, j) in a $P \times Q$ search region in **C**, where $P > L$ and $Q > M$, the SAD coefficients $\epsilon_{i,j}$ are computed:

$$\epsilon_{i,j} = \sum_{\ell=1}^{L} \sum_{m=1}^{M} |C_{\ell,m} - U_{\ell+i,m+j}|. \tag{1}$$

Let $\epsilon_{I,J} = \min\{\epsilon_{i,j}\}$ be the minimum SAD coefficient in the search region. The location of $\epsilon_{I,J}$ identifies the position (z_C, y_C) in **C** that corresponds to (z_U, y_U) in **U**. The displacement vector is:

$$\mathbf{D} = (D_z, D_y) = ((z_C - z_U), (y_C - y_U)) \tag{2}$$

with an uncertainty at least as large as the axial (Δz) and lateral (Δy) sampling intervals.

Since $\Delta y \geq 10\Delta z$, we attempted to interpolate between y displacements for subsample estimates and increased precision. Simple linear interpolation methods produced strong artifacts that were unacceptable. We also tried the technique of Geiman *et al.* [36] to interpolate between echo waveforms based on a ratio of gradients in **U** and **C** around (z_C, y_C). However, the additional derivative made that method more sensitive to noise. Unlike blood velocity imaging, where ensemble averaging is possible, there is

only one pair of noise realizations in strain imaging. Consequently nearest-neighbor interpolation was used.

D. 2-D Global Companding

Sixteen nonoverlapping SAD kernels were equally distributed over **U** at points (z_U, y_U) as shown in Fig. 2(a). From the resultant displacement vectors, 16 corresponding points (z_C, y_C) were estimated. Using linear regression analysis, we solved for the companding parameters m_y and m_z and shift parameters b_y and b_z using the equations:

$$\begin{aligned} z_C &= m_z z_U + b_z \\ y_C &= m_y y_U + b_y. \end{aligned} \tag{3}$$

U was then shifted and scaled accordingly, and the axial companding parameter m_z was added to the strain computed by crosscorrelation to obtain the measured strain.

E. 2-D Local Companding

Many overlapping SAD kernels were applied to **U** as shown in Fig. 2(b) to estimate local displacements in two dimensions. The kernels were separated by five samples along z and one sample along y. Roughly 10^4 estimates were calculated for a 15×15 mm echo field in about 10 minutes on a workstation. Each segment of five vertical samples along U_z was then shifted such that $(U_z, U_y) \longrightarrow (U_{z+D_z}, U_{y+D_y})$. Although echo data were shifted at each kernel location, not scaled, the shifts were spatially varying so the net effect was to locally deform, or compand, **U** to more closely approximate **C**. Displacements along the beam axis were stored and added to those later detected using crosscorrelation.
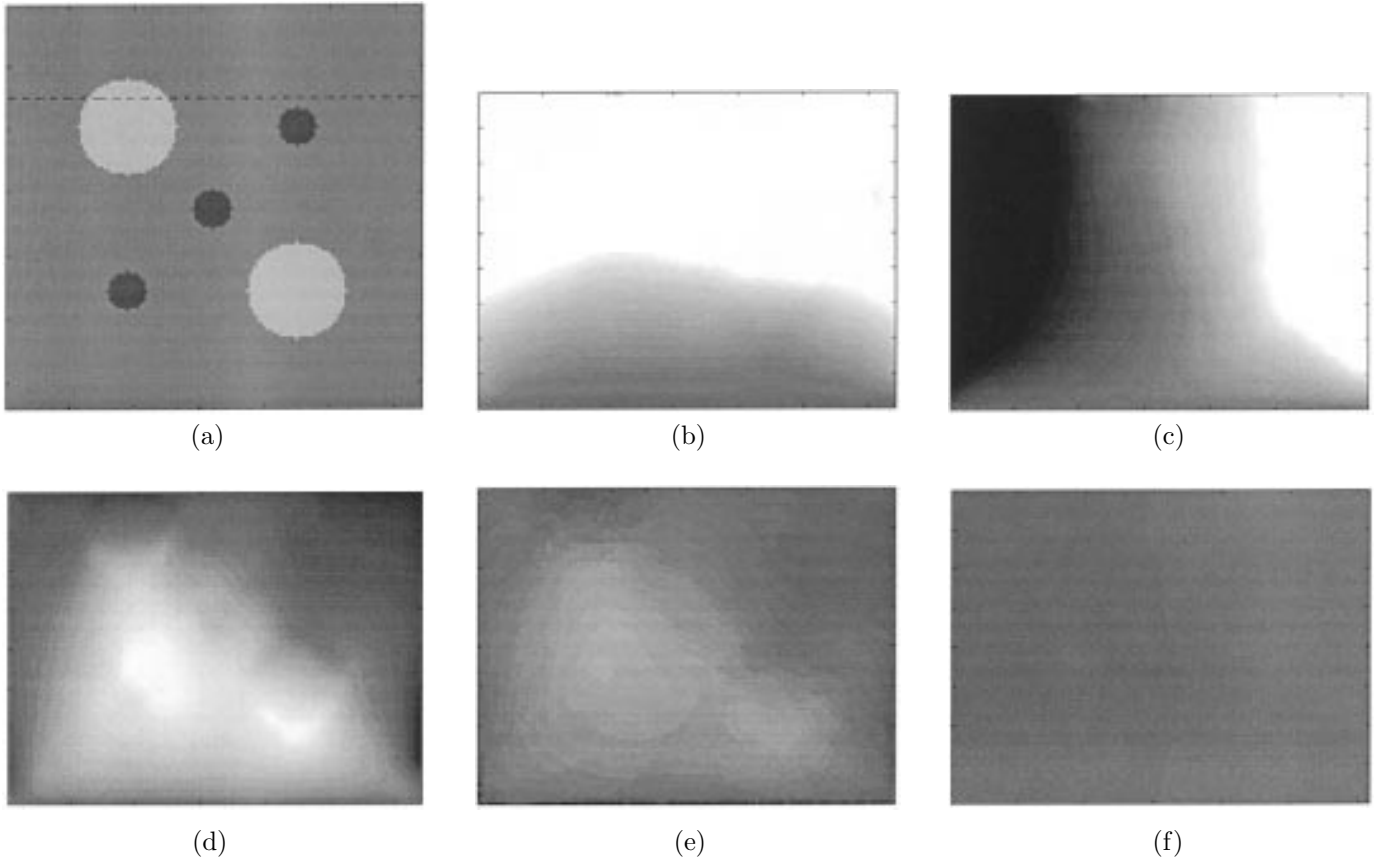
Fig. 3. Demonstration of the effect of companding on displacement. (a) A 2-D elastic modulus field was simulated for an incompressible object. The bright targets are softer than the background and the dark targets are stiffer. The object was compressed uniformly from the top surface, and the bottom surface was bound. Only the region below the dotted line was included in the following displacement images. The longitudinal (b) and transverse (c) displacement fields show regions of large positive (white), zero (gray), and large negative (black) displacements. 1-D global companding along the vertical axis resulted in (d). After 2-D local companding, however, the residual longitudinal (e) and transverse (f) displacements were much smaller than the originals (b) and (c), respectively.

F. An Example

The effects of 2-D global and local companding on displacement are illustrated in Fig. 3 independent of the ultrasound signals. Compression of the 2-D object shown in Fig. 3(a) was simulated using a finite-element analysis (FEA) software package from Algor, Inc. (Pittsburgh, PA) assuming a plane-strain state and linear elastic media. Young's modulus was 100 kPa in the background, 50 kPa in two soft bright targets, and 150 kPa in three hard dark targets. The overall object dimensions in this example were $100 \text{ mm} \times 100 \text{ mm}$, the large targets had a 20 mm diameter, and the small targets had 8 mm diameters. The object was compressed uniformly 10% of its height from the top surface that was allowed to freely slip along the compressor, while the bottom surface was bound in all directions. The longitudinal [Fig. 3(b)] and transverse [Fig. 3(c)] displacement fields show how the elasticity and boundary heterogeneities distort the displacement symmetry. Nonuniform displacements indicate that the object was strained in both dimensions.

After longitudinally stretching the postcompression object (1-D global companding) by exactly the amount of strain applied (d), the steep longitudinal gradient was removed [compare Figs. 3(b) and (d)] but the residual displacement remained nonuniform. Wherever the displacement gradient in Fig. 3(d) is high, time delay estimation involving ultrasound signals will suffer large decorrelation errors. Companding aims to minimize strain over the dimension of the crosscorrelation window, roughly 2 mm.

A random field of points was deformed according to the displacement fields in Figs. 3(b) and (c), and 2-D local companding was applied to measure the displacement. This simulated echo field is equivalent to scanning a random scattering medium with an ideal point impulse response. Although nonphysical, this simulation serves to illustrate object motion without decorrelation errors. The compander output was subtracted from Figs. 3(b) and (c), and the residual longitudinal and transverse displacement fields are displayed in Figs. 3(e) and (f), respectively. Local companding removed nearly all the transverse displacement (its magnitude is only half that in the longitudinal direction) and most of the longitudinal displacement. The advantages of local companding for strain imaging are realized because the strain gradient along the sound beam usually varies much more slowly than the displacement

gradient. Global companding is not essential for successful local companding, although, when they are used together, the total processing time is an order of magnitude less than that using local companding alone.

In Section III, we present the results of several ultrasound simulations and phantom measurements performed with the imaging algorithm outlined in Fig. 1.

III. RESULTS

A. Simulations

Simulation model: Several experiments involved simulated ultrasonic echo data. The precompression rf echo field **U** was simulated by applying the linear model [37],

$$U_{z,y} = G_{z,y} + N_{z,y}. \tag{4}$$

N is a signal-independent white noise process. G is a convolution between the scatterer impulse response and pulse-echo impulse response functions. The latter is a 2-D Gaussian function modulated by a sine wave along the z axis. The former assumes a 3-D field of randomly positioned 100 μm-diameter scatterers having sufficient number density to produce fully developed speckle [37].

The postcompression rf echo field **C** was simulated by deforming an exact copy of the random scatterer field used for **U** according to an FEA model. The object was allowed to slip freely along boundary surfaces. The deformed scatterer field was then convolved with the same pulse-echo impulse response to yield $G'_{z,y}$. Consequently,

$$C_{z,y} = G'_{z,y} + N'_{z,y}, \tag{5}$$

where N' is an independent, identically distributed realization of N.

Paramaters for the simulation model were specified to match the phantom experiments described in the subsection III. B, except that the elevational beam-width was approximately 1.5 mm in the phantom experiment whereas a 2-D beam in the scan plane was used in the simulations. The simulated linear array had a center frequency of 5.0 MHz and a bandwidth of 3 MHz. Waveforms were sampled at 50 MHz to provide 1024 samples per waveform. The scan plane included 128 waveforms separated 0.16 mm with every fourth waveform being uncorrelated. The simulated noise amplitude was 40 dB below that of the signal. The SAD kernel, search region, and correlation window sizes were selected by visual inspection of the images; no attempt at objective optimization was made. A 4 waveform × 50 samples (0.64 × 0.77 mm) SAD kernel was used for local companding in all simulations and phantom experiments except the first simulation experiment, in which a 4 × 30 (0.64 × 0.46 mm) kernel was used. A Hanning-weighted correlation window of 128 samples (2.0 mm) was selected. The vertical shift between adjacent correlation windows (axial pixel dimension) was 16

samples (0.25 mm) resulting in a 92% overlap between windows.

Simulation experiments: In the first simulation experiment, an elastically homogeneous and incompressible 2-D object was compressed 3.1% along the beam axis. Only step 2 from Fig. 1 was applied. The axial and lateral displacements detected by the SAD algorithm are shown in Fig. 4. The 2-D local compander was able to correctly detect this simple motion with little uncertainty, although the higher axial sampling rate resulted in greater precision.

In the second simulation experiment, an inhomogeneous and incompressible 3-D object was compressed 3.1% along the beam axis. The object was a right circular cylinder 15 mm long and 20 mm in diameter (beam and cylinder were coaxial). A 6.5 mm-diameter sphere with a stiffness three times greater than the background was placed at the center of the cylinder. A central cross-section through the object depicting the elastic modulus distribution is shown in Fig. 5(a). The stiff sphere appears dark. The simulated acoustic scattering field was random and uniform throughout, i.e., the sphere provided no acoustic contrast. The cylinder was compressed from below and scanned in the central plane, such that there was no motion out of the image plane. The object strain field found from the gradient of the longitudinal FEA displacement is shown in Fig. 5(b).

The simulated echo fields were analyzed to form longitudinal strain images without [Fig. 5(c)] and with [Fig. 5(d)] local companding. With respect to Fig. 1, steps 1 and 3 were applied in Fig. 5(c), and steps 1, 2, and 3 were applied in Fig. 5(d). Bright pixels represent large strain (soft regions) and dark pixels represent small strain (stiff regions). Without local companding, the decorrelation noise in Fig. 5(c) was obvious. Decorrelation noise was most apparent near the lateral margins where lateral displacements were greatest.

In the third simulation experiment, two stiff spheres were centered on the axis of a background cylinder as shown in cross-section in Fig. 6(a). Other object parameters were the same as in simulation experiment 2. The sphere diameters were 2 and 4 mm. Stress concentrations distort the circular shape of the targets as seen in the object strain field, Fig. 6(b). Longitudinal strain images without and with local companding are shown in Figs. 6(c) and (d), respectively. Global companding was applied in both cases. Fig. 6(e) shows the strain image obtained from the displacement estimates provided by the local compander without correlation (steps 1 and 2 only). The targets are most visible in the images where all three steps—global companding, local companding, and correlation—were applied.

In the fourth simulation experiment, the object in Fig. 6(a) was again analyzed, except that the transverse strain was imaged. That is, the object, now shown in Fig. 7(a), was compressed from the right along the axis of the cylinder but scanned from above. The strain field in tension is shown in Fig. 7(b). The stiff targets appear
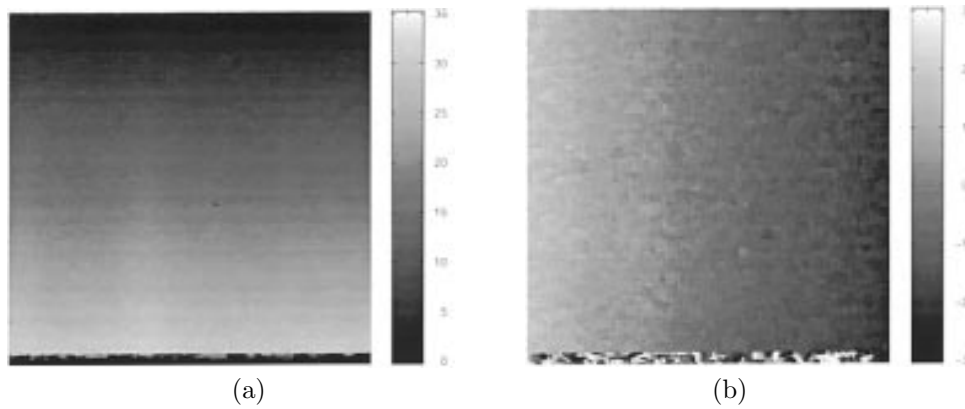
Fig. 4. Axial (a) and lateral (b) displacement fields in the scan plane as detected by the SAD algorithm for simulated ultrasonic echo fields of an elastically homogeneous medium compressed 3.1% from the bottom surface. This is a 2-D FEA model under plane-strain with free-slip boundary conditions. Notice the greater noise for lateral displacements (b) as compared with axial displacement (a).
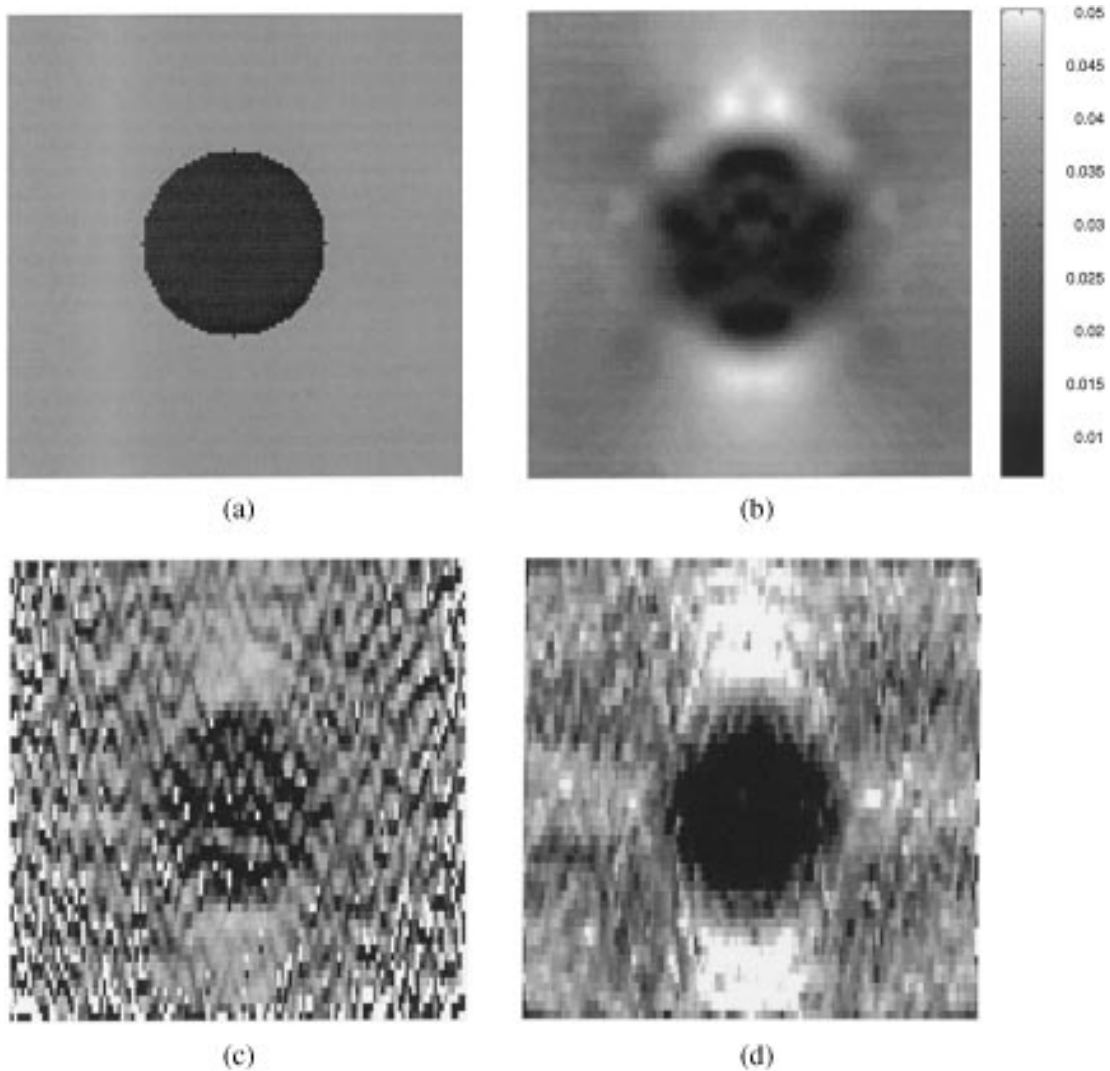

Fig. 5. Longitudinal strain images. The elastic modulus distribution (a), object strain field (b), and strain images (c) and (d) of a spherical target 6.5 mm in diameter and three times stiffer than the background. Strain images were formed without (c) and with (d) local companding (step 2 in Fig. 1.) The object was compressed 3.1% from below.
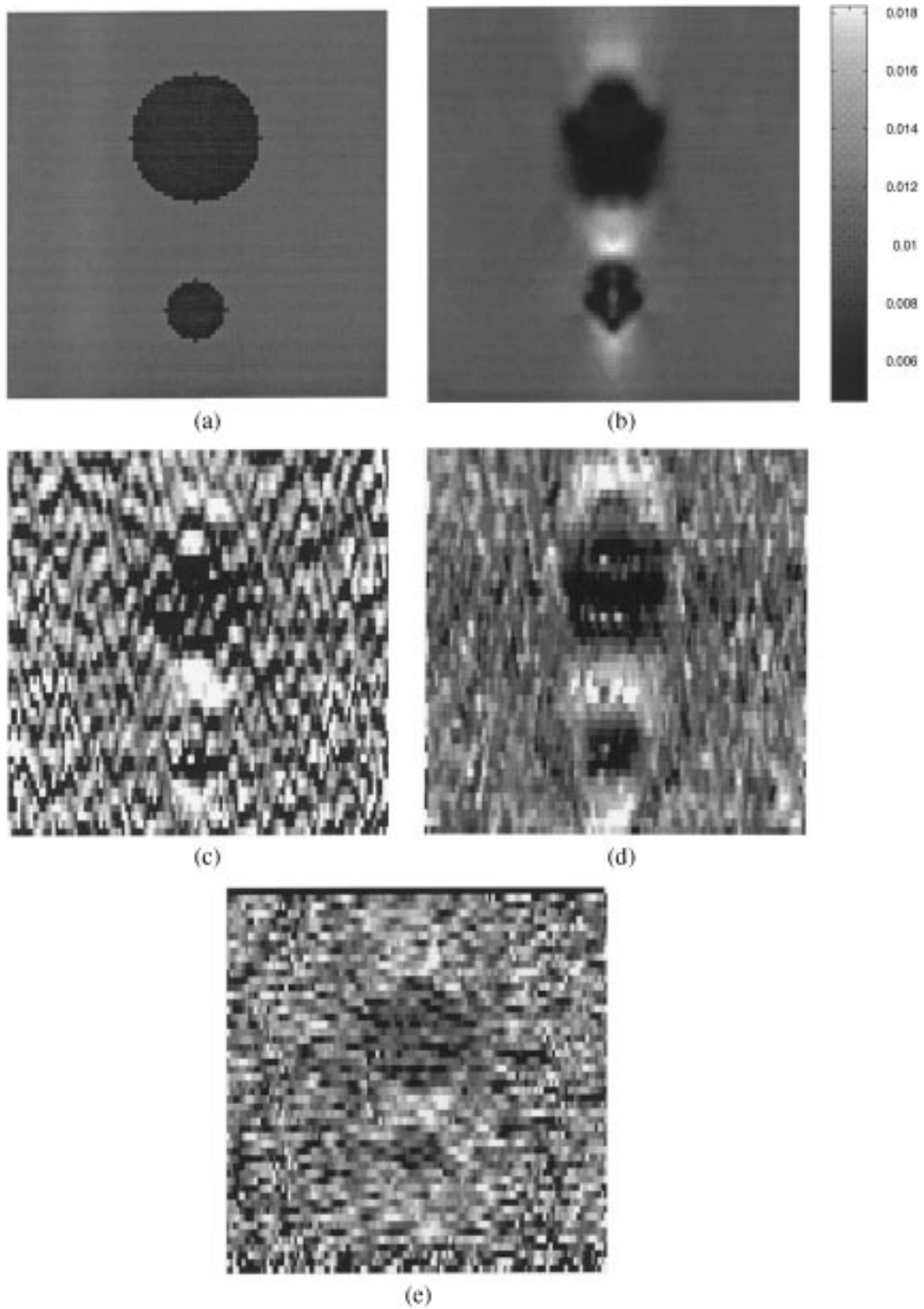
Fig. 6. Longitudinal strain images. The elastic modulus distribution (a), object strain field (b), and reconstructed strain images (c)–(e) of two stiff spherical targets of diameters of 2 and 4 mm. Referring to Fig. 1, strain images were formed using steps 1 and 3 (no local companding) in (c), steps 1, 2, and 3 in (d), and steps 1 and 2 (no correlation) in (e). The object was compressed 3.1% from below and scanned along the direction of compression.
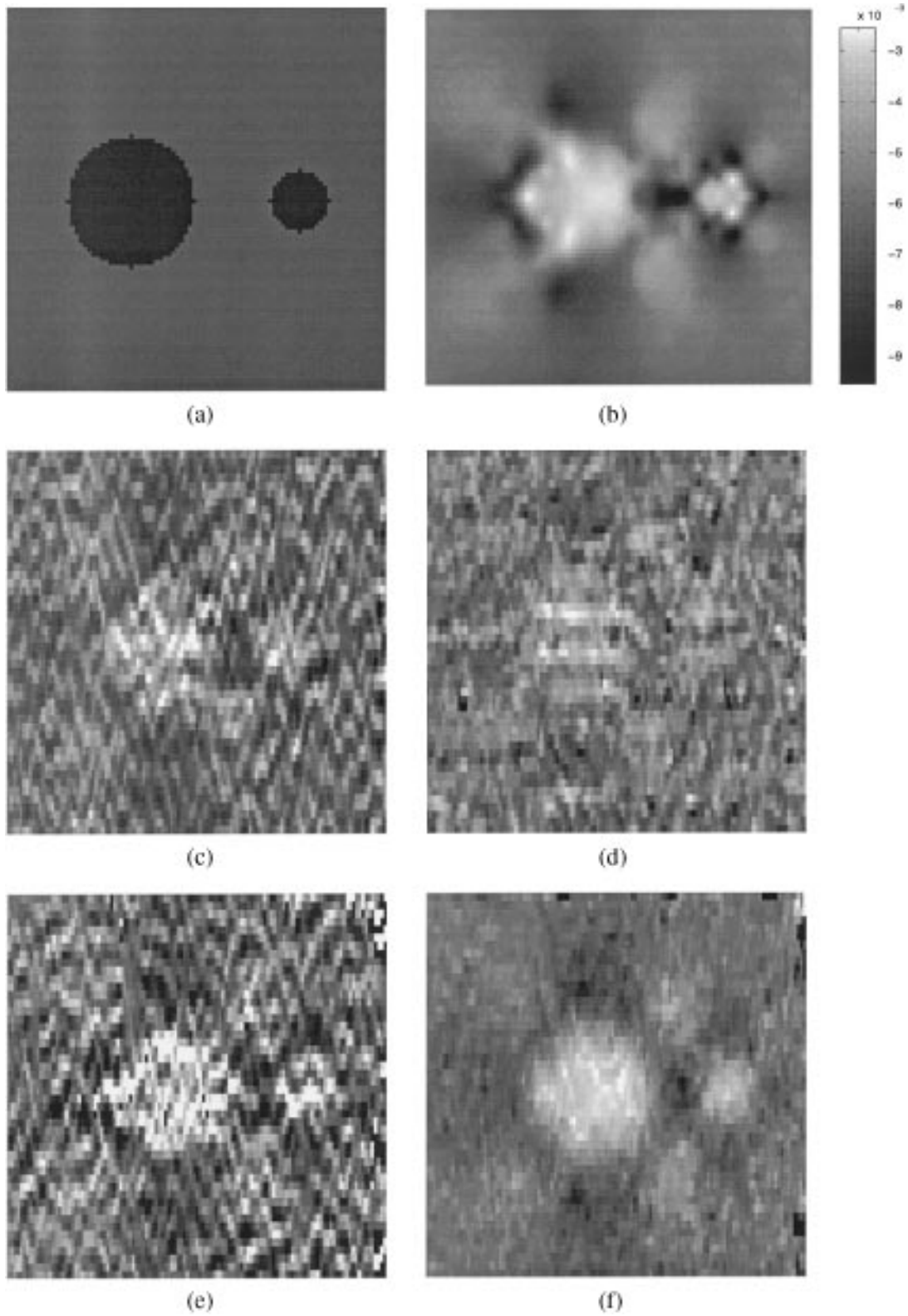
Fig. 7. Transverse strain images of the object in Fig. 6(a). In this experiment, the object was compressed from the right and scanned from below. The object strain field is shown in (b) and strain images in (c)–(f). The object was compressed 3.1% in (c) and (d) and 15.5% in (e) and (f). The strain values depicted in (e) and (f) are five times the values in (b)–(d). Local companding was not applied in (c) and (e) but was applied in (d) and (f).
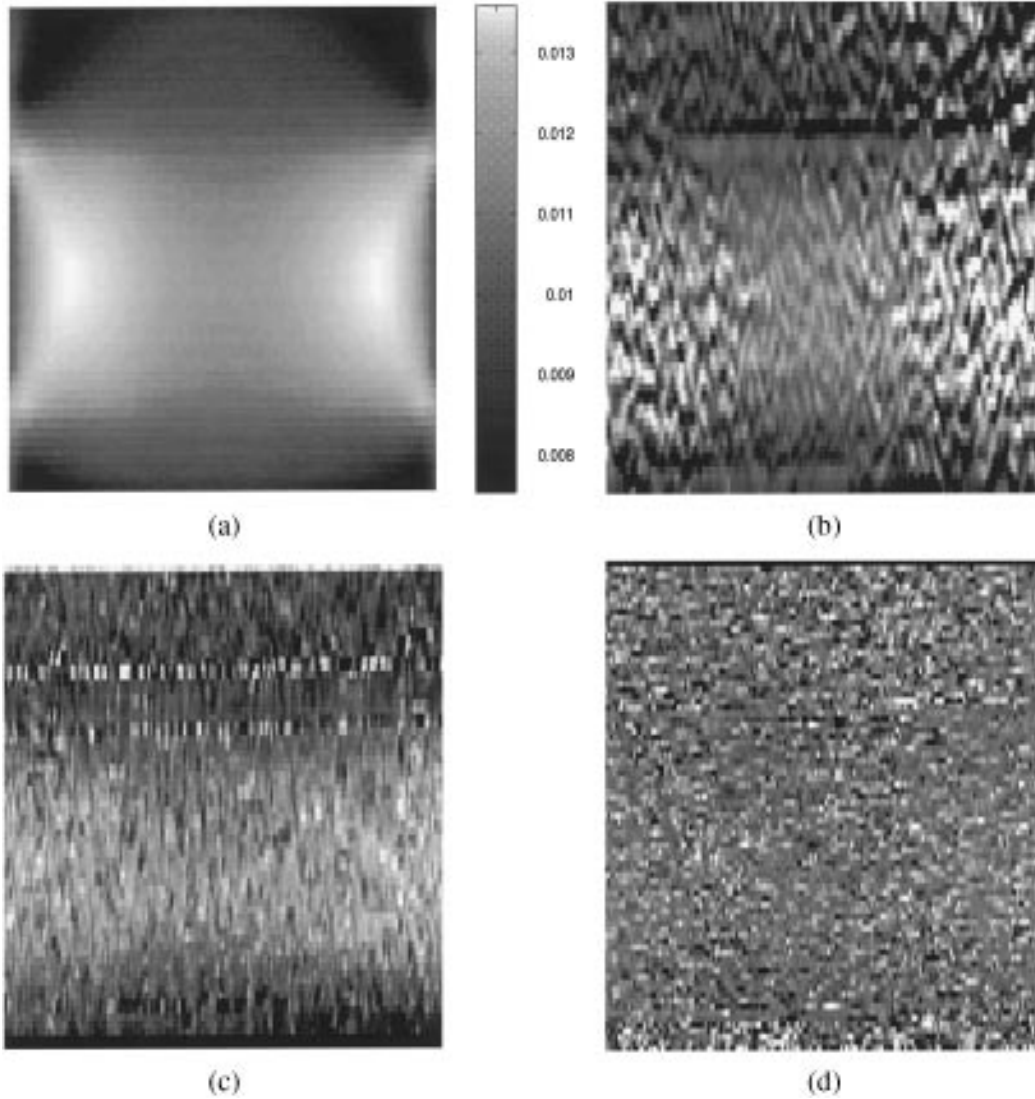
Fig. 8. Longitudinal strain images of a 3-layer graphite gel phantom. The middle layer had approximately half the stiffness of the other layers. (a) is the object strain field modeled using FEA when the phantom is physically constrained so that all the motion is in the scan plane. (b)–(d) are the strain images measured using a 5 MHz linear array. Referring to Fig. 1, strain images were formed using steps 1 and 3 (no local companding) in (b), steps 1, 2, and 3 in (c), and steps 1 and 2 (no correlation) in (d).

brighter than the background because the strain is negative in tension. Compressing the object 3.1% resulted in Figs. 7(c) and (d). Local companding reduced noise and contrast as seen in Fig. 7(d). Since transverse displacements were only 50% of the longitudinal displacement for the incompressible cylinder used in this simulation, the signal-to-noise ratio for transverse strain estimates in Fig. 7(d) was lower than that for longitudinal strain estimates in Fig. 6(d). Target visibility was contrast limited in the transverse strain images of Figs. 7(c) and (d) and noise limited in the longitudinal strain images of Figs. 6(c) and (d). We restored the noise-limited condition to transverse strain images by compressing the object 15.5%. The results, shown in Figs. 7(e) and (f), indicate that companding is most effective in noise-limited imaging situations. The position of the scan planes were chosen so there was no out-of-plane displacement, allowing relatively

large compressions to be applied without decorrelation. It is particularly important to apply global companding in two dimensions for transverse strain images, because lateral displacements are much greater than axial.

To compare target visibility for images formed with and without local companding, the following contrast-to-noise ratio was computed:

$$\text{CNR} = \sqrt{\frac{2(\bar{s}_t - \bar{s}_b)^2}{\text{var}s_t + \text{var}s_b}}. \tag{6}$$

The quantities $\bar{s}$ and var s denote the mean and variance of the strain estimates, and subscripts b and t represent the background and the target, respectively. Mean and variance for the background were computed from a region in the upper left corner of the images, which was relatively free from stress concentration artifacts. Comparison of the CNR for various simulation experiments is provided

TABLE I
CNR IN IMAGES OBTAINED FOR THE SIMULATIONS DESCRIBED IN SECTION III.

Figure	Target	CNR	Figure	Target	CNR
5c	large	0.1183	7c	large	1.2850
5d	large	6.1410		small	1.0128
6c	large	0.0693	7d	large	1.2897
	small	0.1068		small	0.4978
6d	large	2.7669	7e	large	0.5124
	small	2.7138		small	1.0789
6e	large	0.4294	7f	large	7.5324
	small	0.3980		small	5.6282

in Table I. These CNR values are not intended to be rigorous comparisons of lesion detectability. Rather, they are a means to quantify visual impressions independent of the display contrast and brightness settings.

B. Phantom Experiment

We further investigated the advantages of companding by studying strain images of a rectangular graphite-gel phantom constructed with three horizontal layers. The middle layer was approximately half as stiff as the upper and lower layers. The system parameters are the same as those described in subsection III.A for the simulations. The phantom was compressed from the top to produce 1.2% strain in the central layer and scanned from the top with the image plane bisecting the phantom. Data were collected for two sets of boundary conditions: first, the plane strain where both axial and lateral displacements (condition A) were allowed and second when only axial displacements were allowed (condition B). For boundary conditions (A), the object strain obtained by FEA is shown in Fig. 8(a) and the measured strain images are shown in Figs. 8(b)–(d).

Normalized displacement variances were also measured for two of the images in Fig. 8 and displayed in Fig. 9 as a function of correlation window duration T. Axial displacement variances corresponding to the central layer of the phantom imaged in Fig. 8(b) are plotted in Fig. 9 as curve A, indicating the boundary conditions (A). When companding is applied, as in the image of Fig. 8(c), displacement variance is reduced (curve C in Fig. 9) to nearly match the variance for boundary conditions (B), where there is only axial displacement. The three curves of Fig. 9 show that companding eliminates most of the displacement variance caused by decorrelation from lateral tissue motion without adding a significant amount of noise. Furthermore, the reduction in variance is nearly two orders of magnitude. In each situation, displacement variances decreased for long duration windows because the strain was small (1.2%). The exception was for curve A at short duration windows, where the maximum possible variance was obtained, $\mathrm{var}(D_z)/T^2 = 1/12$.
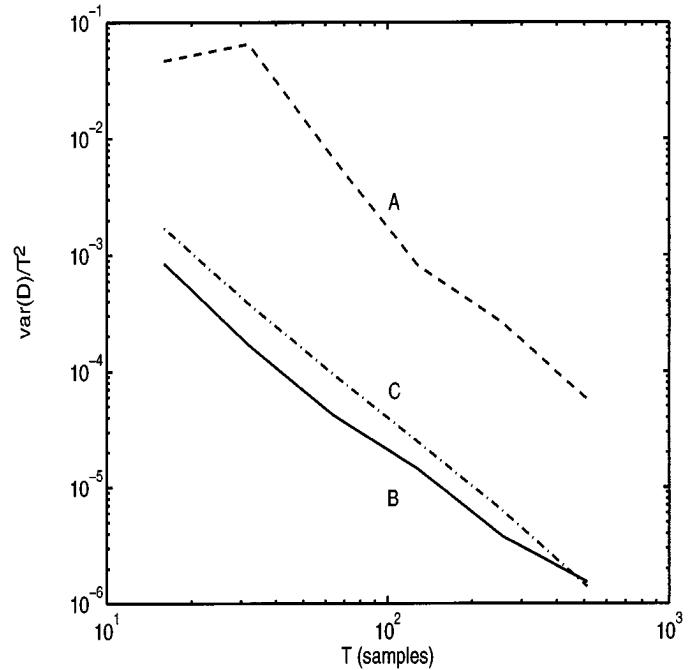

Fig. 9. Plots of correlation window length T vs. normalized displacement variance/T^2 measured for the phantom images of Fig. 8. The strain in the middle layer was 1.2%. "A" indicates the measured variance for plane-strain conditions. "B" indicates the measured variance for axial motion only. "C" indicates the measured variance for data in "A" after 2-D local companding.

IV. DISCUSSION

Results of the simulation experiment of Fig. 4 demonstrate the ability of the SAD algorithm to track simple motion in the image plane. The 3.1% compression applied along the beam in this experiment results in the largest axial motion (at the bottom) of 32 samples and lateral motion of ±2 rf lines. These features are clearly reflected in the images shown in Fig. 4 because there is little signal decorrelation. The small amount of data lost near the bottom of each image in all experiments is the result of new regions moving into the scan plane during compression.

The addition of local companding to correlation-based strain imaging for measuring complex movement within inhomogeneous objects is illustrated in Figs. 5–7. Local companding reduced lateral decorrelation, produced spatially uniform strain noise, and improved target visibility.
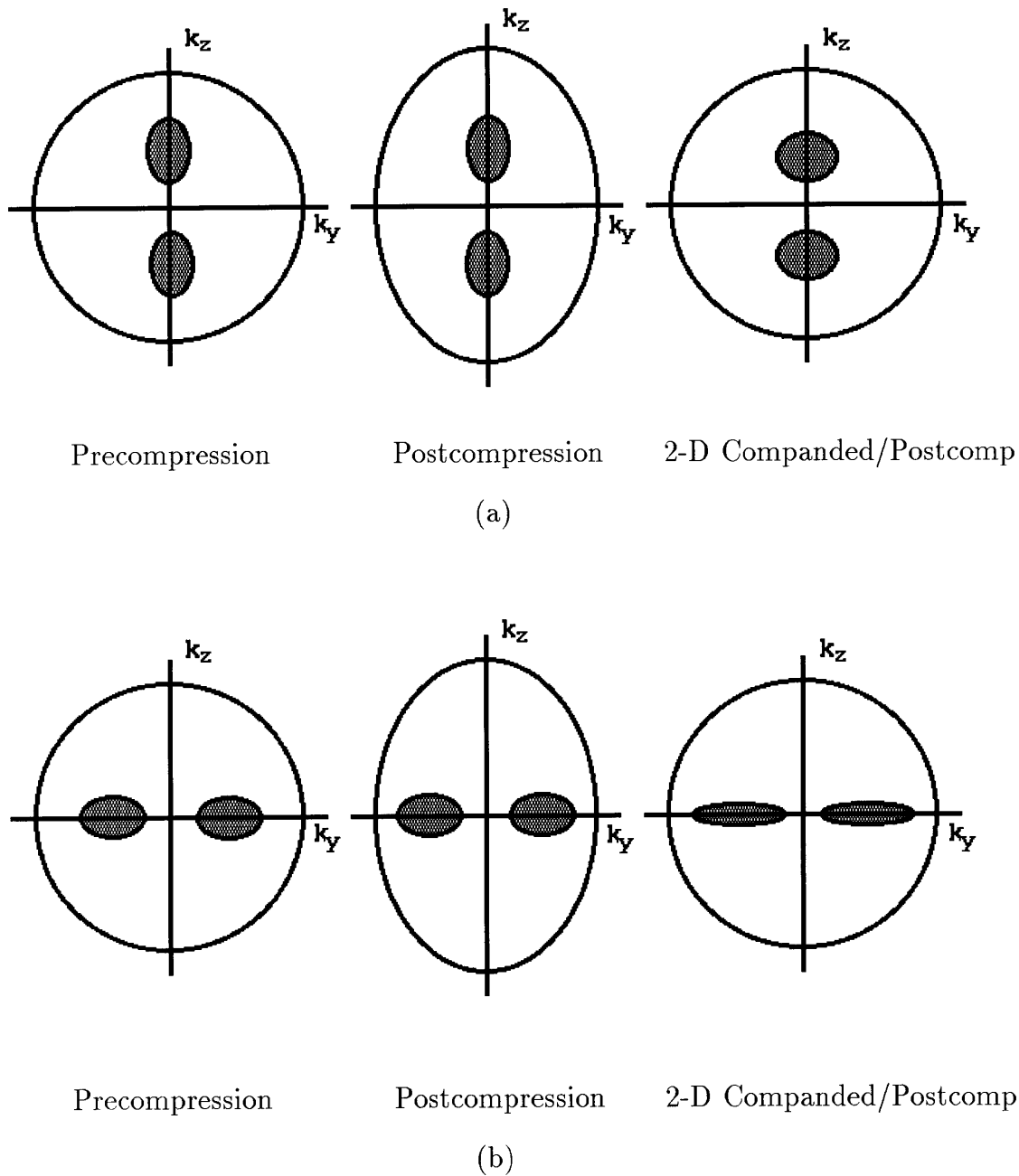
Fig. 10. K-space representation of the pre- and postcompression echo data for longitudinal (a) and transverse (b) strain images. The shaded region represents the pulse spectrum, and the outer circle (ellipse) represents the object spectrum.

The improvements were quantified by the increase in CNR shown in Table I. Companding is only effective at tracking displaced echoes that remain coherent after compression. Out-of-plane motion, for example, cannot be tracked unless the echo data are finely sampled in three dimensions.

Simulation experiments with the two-target object, Fig. 6, further illustrate the advantages of local companding for more complex object geometries. The image in Fig. 6(c) was obtained with correlation analysis following global companding. The high noise level significantly reduces the visibility of the smaller target. With 2-D local companding followed by crosscorrelation, the strain noise in Fig. 6(d) is greatly reduced, and both targets closely re-

semble those in the object strain, Fig. 6(a). Strain images obtained by 2-D local companding without crosscorrelation, e.g., Fig. 6(e), exhibit higher noise and lower contrast when compared to Fig. 6(d). Therefore, companding itself does not improve image quality significantly. All three steps in displacement estimation summarized in Fig. 1 are needed for efficient strain imaging.

Transverse strain images have less noise than longitudinal strain images under the conditions that exist in the simulation experiment for a fundamental reason that is illustrated in the *k*-space diagrams [29], [38] of Fig. 10. Fig. 10(a) shows ensemble tissue and pulse-echo spectra for precompression, postcompression, and 2-D com-

panded/postcompression echo data of a hypothetical tissue sample. k_y and k_z represent components of the wavevector perpendicular and parallel to the compression axis, respectively. A broadband pulse propagating along z (shaded areas) is used to probe a very broadband object with a circular k-space representation that contains many spatial frequencies not included in the pulse bandwidth. The product of the pulse and tissue spectra determines which tissue structures are visible to the ultrasound system.

Strain of the incompressible tissue along z elongates the symmetric tissue spectrum along k_z and narrows it along k_y, forming an ellipse. The deformed object is then scanned with the same pulse. Successful 2-D global companding restores the tissue spectrum but deforms the pulse spectrum such that the spatial frequencies probed before compression are not the same as those after compression. The deformation reduced the center frequency and bandwidth of the pulse along k_z. The loss of signal coherence ultimately degrades the CNR for strain images.

In transverse strain images, however, 2-D global companding increased the center frequency and bandwidth of the echo signal as diagrammed in Fig. 10(b). There is greater overlap between the pre- and postcompression echo spectra and, therefore, less decorrelation noise.

Images of the three-layer graphite-gel phantom provide experimental evidence in support of employing local companding. The image obtained without 2-D local companding displayed large strain noise near the lateral margins [Fig. 8(b)]. The object strain contributed only a small fraction of the image variability, as seen by a comparison with Fig. 8(a). The decorrelation noise added by lateral motion was reduced by local companding [Fig. 8(c)]. However, the algorithm was less successful near the layer boundaries. There are two possible reasons for the enhanced noise at the boundaries. First, imperfect bonding between phantom layers can cause slippage resulting in large local displacements. Second, the gradient operation used for computing strain from displacement exacerbates the noise added by the SAD algorithm near boundaries, resulting in a process similar to edge-detection.

2-D local companding increased the total processing time for strain image formation. The amount of time depends on the sizes of the image, SAD kernel, and search region. Image formation can take anywhere between a few minutes to a few hours on a DEC-Alpha workstation. It is expected that local companding using the SAD algorithm can be accomplished at near real-time rates using DSP technology [35].

V. Conclusions

A 2-D local companding technique for reducing noise in strain images is presented. By companding the data prior to using crosscorrelation to compute strain, image noise is reduced by two orders of magnitude or more. However, since strain variance increases with the applied strain, there are limits to the effectiveness of companding that have yet to be explored.

The relatively large compressions that must be applied to realize the improved target visibility of strain images also increase the chances for decorrelation from out-of-plane motion. If boundary conditions can be established that restrict motion to the scan plane, then large compressions increase signal strength (strain contrast) and target visibility is noise limited. Under those conditions, local companding is most useful.

References

[1] L. S. Wilson and D. E. Robinson, "Ultrasonic measurement of small displacements and deformations of tissues," *Ultrason. Imaging*, vol. 4, pp. 71–82, 1982.

[2] M. Tristam, D. C. Barbosa, D. O. Cosgrove, D. K. Nassiri, J. C. Bamber, and C. R. Hill, "Ultrasonic study of in vivo kinetic characteristics of human tissues," *Ultrason. Med. Biol.*, vol. 12, pp. 927–937, 1986.

[3] T. A. Krouskop, D. R. Dougherty, and S. F. Vinson, "A pulsed Doppler ultrasonic system for making non-invasive measurements of the mechanical properties of soft tissues," *J. Rehab. Res. Dev.*, vol. 24, pp. 1–8, 1987.

[4] Y. Yamakoshi, J. Sato, and T. Sato, "Ultrasonic imaging of internal vibration of soft tissue under forced vibration," *IEEE Trans. Ultrason., Ferroelect., Freq. Contr.*, vol. 37, pp. 45–53, 1990.

[5] R. M. Lerner, S. R. Huang, and K. J. Parker, "*Sonoelasticity* images for ultrasound signals in mechanically vibrated tissues," *Ultrason. Med. Biol.*, vol. 16, pp. 231–239, 1990.

[6] J. Ophir, I. Céspedes, H. Ponnekanti, Y. Yazdi, and X. Li, "Elastography: quantitative method for imaging the elasticity of biological tissue," *Ultrason. Imaging*, vol. 13, pp. 111–134, 1991.

[7] B. S. Garra, I. Céspedes, J. Ophir, S. R. Spratt, R. A. Zuurbier, C. M. Magnant, and M. F. Pennanen, " Elastography of breast lesions: initial clinical results," *Radiology*, vol. 202, pp. 79–86, 1997.

[8] M. O'Donnell, A. R. Skovoroda, B. M. Shapo, and S. Y. Emelianov, "Internal displacement and strain imaging using ultrasonic speckle tracking," *IEEE Trans. Ultrason., Ferroelect., Freq. Contr.*, vol. 41, pp. 314–325, 1994.

[9] A. R. Skovoroda, S. Y. Emelianov, M. A. Lubinski, A. P. Sarvazyan, and M. O'Donnell, "Theoretical analysis and verification of ultrasound displacement and strain imaging," *IEEE Trans. Ultrason., Ferroelect., Freq. Contr.*, vol. 41, pp. 302–313, 1994.

[10] C. Sumi, A. Suzuki, and K. Nakayama, "Estimation of shear modulus distribution in soft tissue from strain distribution," *IEEE Trans. Ultrason., Ferroelect., Freq. Contr.*, vol. 42, pp. 193–202, 1995.

[11] E. J. Chen, R. S. Adler, P. L. Carson, W. K. Jenkins, and W. D. O'Brien, "Ultrasound tissue displacement imaging with application to breast cancer," *Ultrason. Med. Biol.*, vol. 21, pp. 1153–1162, 1995.

[12] L. Gao, K. J. Parker, R. M. Lerner, and S. F. Levinson, "Imaging of the elastic properties of the tissue: A review," *Ultrason. Med. Biol.*, vol. 22, pp. 959–977, 1996.

[13] R. Muthupillai, D. J. Lomas, P. J. Rossman, J. F. Greenleaf, A. Manduca, and R. L. Ehman, "Magnetic resonance elastography by direct visualization of propagating acoustic strain waves," *Science*, vol. 269, pp. 1854–1857, 1995.

[14] A. P. Sarvazyan, A. R. Skovoroda, S. Y. Emelianov, J. B. Fowlkes, J. G. Pipe, R. S. Adler, R. B. Buxton, and P. L. Carson, "Biophysical bases of elasticity imaging," *Acoust. Imaging*, vol. 21, pp. 223–240, 1995.

[15] K. Motoi, H. Morita, N. Fujita, Y. Takano, K. Muzushige, S. Senda, and H. Matsuo, "Stiffness of human arterial wall assessed by intravascular ultrasound," *J. Cardiol.*, vol. 25, pp. 189–197, 1995.

[16] I. Céspedes and J. Ophir, "Reduction of image noise in elastography," *Ultrason. Imaging*, vol. 15, pp. 89–102, 1993.

[17] S. K. Alam and J. Ophir, "Reduction of signal decorrelation from mechanical compression of tissues by temporal stretching: applications to elastography," *Ultrason. Med. Biol.*, vol. 23, pp. 95–105, 1997.

[18] M. Bilgen and M. F. Insana, "Error analysis in acoustic elastography. I. Displacement estimation, and II. Strain estimation and SNR analysis," *J. Acoust. Soc. Amer.*, vol. 101, pp. 1139–1154, 1997.

[19] W. R. Remley, "Correlation of signals having a linear delay," *J. Acoust. Soc. Amer.*, vol. 35, pp. 65 and 69, 1963.

[20] C. H. Knapp and G. C. Carter, "Estimation of time delay in the presence of source or receiver motion," *J. Acoust. Soc. Amer.*, vol. 70, pp. 1545–1549, 1977.

[21] W. B. Adams, J. P. Kuhn, and W. P. Whyland, "Correlator compensation requirements for passive time-delay estimation with moving sources or receivers," *IEEE Trans. Acoust., Speech, Signal Processing*, vol. 28, pp. 158–168, 1980.

[22] J. W. Betz, "Comparison of the deskewed short-time correlator and the maximum-likelihood correlator," *IEEE Trans. Acoust., Speech, Signal Processing*, vol. 32, pp. 285–294, 1984.

[23] J. W. Betz, "Effects of uncompensated relative time companding on a broad-band cross correlator," *IEEE Trans. Acoust., Speech, Signal Processing*, vol. 33, pp. 505–510, 1985.

[24] T. Varghese, J. Ophir, and I. Céspedes, "Noise reduction in elastograms using temporal stretching with multicompression averaging," *Ultrason. Med. Biol.*, vol. 22, pp. 1043–1052, 1996.

[25] M. A. Lubinski, S. Y. Emelianov, K. R. Raghavan, A. E. Yagle, A. R. Skovoroda, and M. O'Donnell, "Lateral displacement estimation using tissue incompressibility," *IEEE Trans. Ultrason., Ferroelect., Freq. Contr.*, vol. 43, pp. 247–255, 1996.

[26] I. Céspedes, Y. Huang, J. Ophir, and S. Spratt, "Methods for estimation of subsample time delays of digitized echo signals," *Ultrason. Imaging*, vol. 17, pp. 142–171, 1995.

[27] M. Bilgen and M. F. Insana, "Deformation models and correlation analysis in elastography," *J. Acoust. Soc. Amer.*, vol. 99, pp. 3212–3224, 1996.

[28] J. Meunier, M. Bertrand, and G. Mailloux, "A model for dynamic texture analysis in two-dimensional echocardiograms of the myocardium," *Proc. SPIE*, vol. 768, pp. 193–200, 1987.

[29] F. Kallel, M. Bertrand, and J. Meunier, "Speckle motion artifact under tissue rotation," *IEEE Trans. Ultrason., Ferroelect., Freq. Contr.*, vol. 41, pp. 105–122, 1994.

[30] F. Kallel and J. Ophir, "Three-dimensional tissue motion and its effect on image noise in elastography," *IEEE Trans. Ultrason., Ferroelect., Freq. Contr.*, vol. 44, pp. 1286–1296, 1997.

[31] S. Y. Emelianov, M. A. Lubinski, W. F. Weitzel, R. C. Wiggins, A. R. Skovoroda, and M. O'Donnell, "Elasticity imaging for early detection of renal pathology," *Ultrason. Med. Biol.*, vol. 21, pp. 871–883, 1995.

[32] E. E. Konofagou and J. Ophir, "Techniques for expansion of dynamic range in elastography: theory and application," *Ultrason. Imaging*, vol. 18, p. 64, 1996 (Abstr.).

[33] M. F. Insana, M. Bilgen, P. Chaturvedi, T. J. Hall, and M. Bertrand, "Signal processing strategies in acoustic elastography," *Proc. IEEE Ultrason. Symp.*, 1997, pp. 1139–1142.

[34] L. N. Bohs and G. E. Trahey, "A novel method for angle independent ultrasonic imaging of blood flow and tissue motion," *IEEE Trans. Biomed. Eng.*, vol. 38, pp. 280–286, 1991.

[35] L. N. Bohs, B. H. Friemel, B. A. McDermott, and G. E. Trahey, "A real time system for quantifying and displaying two-dimensional velocities using ultrasound," *Ultrason. Med. Biol.*, vol. 19, pp. 751–761, 1994.

[36] B. J. Geiman, L. N. Bohs, M. E. Anderson, S. P. Czenszak, and G. E. Trahey, "2D vector flow imaging using ensemble tracking: initial results," *Ultrason. Imaging*, vol. 18, pp. 61–62, 1996, (Abstr.).

[37] P. Chaturvedi and M. F. Insana, "Error bounds on ultrasonic scatterer size estimates," *J. Acoust. Soc. Amer.*, vol. 100, pp. 392–399, 1996.

[38] R. M. Lerner and R. C. Waag, "Wavespace interpretation of scattered ultrasound," *Ultrason. Med. Biol.*, vol. 14, pp. 97–102, 1988.

Pawan Chaturvedi (S'91–M'92–S'93–M'95) was born in Katni, India on January 21, 1968. He received the B.Sc. (Honors) degree in physics from the University of Delhi in 1988, M.Sc. in physics from the Indian Institute of Technology, Delhi in 1990, M.S. in electrical engineering from Tulane University, New Orleans in 1992, and a Ph.D. in electrical engineering from the University of Kansas in 1995. During the summer of 1989, he was a visiting researcher at the Tata Institute of Fundamental Research, Bombay. From 1990 to 1995 he held teaching and research assistant positions at Tulane University and the University of Kansas. Since 1995, he has been with the Department of Radiology at the University of Kansas Medical Center in Kansas City, where he is currently an Assistant Professor. His research interests are primarily in the fields of inverse problems, acoustic and electromagnetic imaging, and signal and image processing. He is a member of IEEE, Tau Beta Pi, Eta Kappa Nu and Phi Beta Delta.

Michael F. Insana (M'85) was born in Portsmouth, VA on December 18, 1954. He received the B.S. degree in physics from Oakland University, Rochester, MI in 1978 and the M.S. and Ph.D. degrees in medical physics from the University of Wisconsin, Madison, WI in 1982 and 1983, respectively. From 1984 to 1987 he was a research physicist at the FDA's Center for Devices and Radiological Health, where he worked in medical imaging with emphasis on acoustic signal processing. He is currently Associate Professor of Radiology at the University of Kansas Medical Center. His current research interests are acoustic imaging and tissue characterization, signal detection and estimation, observer performance measurements, and image quality assessment. He is a member of the IEEE, SPIE, ASA, AIUM, and AAPM professional societies.

Timothy J. Hall (M'88) received a B.A. in physics from the University of Michigan-Flint in 1983, and M.S. and Ph.D. in Medical Physics from the University of Wisconsin-Madison in 1985 and 1988, respectively.

He is currently an Associate Professor in the Department of Radiology at The University of Kansas Medical Center. Dr. Hall's research interests include quantitative ultrasonic and elastographic imaging, and measures of observer performance and image quality.

Dr. Hall is a member of the IEEE, the Acoustical Society of America, and the American Association of Physicists in Medicine.